Journal of Applied Fluid Mechanics, Vol. 18, No. 11, pp. 2711-2729, 2025.
Available online at www.jafmonline.net, ISSN 1735-3572, EISSN 1735-3645.
https://doi.org/10.47176/jafm.18.11.3564

Erosion Wear and Flow Characteristics of Tri-eccentric Butterfly Valves under Liquid–solid Two-phase Flow

X. L. Yang[1], Y. J. Lü[1†], L. Xu[1,2], Y. S. Ma[1,2], R. B. Chen[1] and Q. A. Li[1]

[1] *School of Mechanical and Precision Instrument Engineering, Xi'an University of Technology, Xi'an 710048, China*
[2] *Liupanshan Laboratory, Yinchuan 750000, China*

†*Corresponding Author Email: yanjunlu@xaut.edu.cn*

ABSTRACT

Excellent sealing performance drives the tri-eccentric butterfly valve's extensive adoption across wastewater treatment sector. Erosion wear is an important cause of leakage and damage in tri-eccentric butterfly valves. Valve surface erosion is affected by the vorticity, particle shape, velocity, and other factors. This paper uses the Computational Fluid Dynamics–Discrete Element Method (CFD-DPM) to build an erosion model based on the Erosion-Corrosion Research Center (E/CRC) methodology, investigating the valve opening's influence on erosion rates under sand particle flow conditions. The two-way coupling phase interaction, wall roughness, particle diameter distribution, and particle geometry are considered in the proposed erosion model. The numerical model is validated through wear and flow experiments. Moreover, the vorticity and velocity correlation coefficients are investigated, with those in the valve stem region exceeding 0.9. The influence of vortex core regions on particle trajectories is investigated, revealing that the velocity angle approaches ±90° in vortex core regions. The numerical results indicate that the sealing surface is particularly vulnerable to wear from particle erosion, exhibiting a peak value of 8.53×10^{-7} $kg\cdot m^{-2}\cdot s^{-1}$. Additionally, wall erosion rate is influenced by vorticity, which alters the angular velocity of solid particles and affects vortex formation.

Article History

Received March 26, 2025
Revised June 3, 2025
Accepted June 29, 2025
Available online September 3, 2025

Keywords:

Tri-eccentric butterfly valve
Erosion wear
Computational fluid dynamics–discrete element method vorticity
Sealing surface

1. INTRODUCTION

Tri-eccentric butterfly valves have better sealing performance than centerline butterfly valves do. Butterfly valve performance is affected by erosion wear resulting from friction and impact between solid particles and valves (Shokri et al., 2017; Javaheri et al., 2018; Tarodiya & Levy 2021; Zhang et al., 2024a; Khan et al., 2024; Perera et al., 2024; Xiong et al., 2024). Particle erosion wear is an important cause of leakage and damage in butterfly valves. Understanding the wear characteristics under liquid-particle conditions proves essential for the tri-eccentric butterfly valve. (Sun et al., 2017; Li et al., 2023; Gao et al., 2024; Guan et al., 2024; Jin et al., 2024a; Kang et al., 2024a).

The control valve erosion has been investigated with the computational fluid dynamics approach (Kang et al., 2024b). Lin et al. (2022) studied how particle diameter influences ball valve wear. The numerical results revealed that wall erosion gradually decreases with increasing particle diameter at small opening degrees. The sealed ball valve's wear characteristics are analyzed using the discrete phase method (Wang et al. 2024) They noted that vortices could lead to erosion on the downstream wall. Xu et al. (2021) investigated the centerline butterfly valve's erosion and reported that erosion is related to high-speed jets. The authors considered that the wear by sharp particles needs to be further investigated. To reduce elbow erosion in a coal gasification system, the erosion characteristics of different types of elbows were investigated, and a novel sheet structure was designed to change the particle position by Wen et al. (2024). More recently, the effect of valves on pipeline flow characteristics have been studied by many scholars. Su et al. (2024) studied pipeline thinning via the CFD method. These works revealed that the higher the velocity of the vortex is, the more severe the corrosion. Chen et al. (2025) examined ball valve erosion and reported that severe erosion occurs more easily with smaller valve openings. Liu et al. (2024a) studied the hydraulic servo pool valve wear patterns and introduced an innovative method to reduce erosion. Owing to erosion mechanisms, the effects of the rotational characteristics of fluid on erosion need to be further investigated.

Yan et al. (2024) developed a predictive model for gate valve erosion rates and reported that sealing surface's erosion decreases with increasing valve opening. Zhang et al. (2024b) investigated how valve seat shape affects slurry valve erosion. Their research has shown that the sealing ring wear is remarkably impacted by the particle diameter and the inner angle. Veiskarami & Saidi (2024) studied the wear mechanism of different geometries as alternatives to the pipe elbow and reported that the central spherical elbow exhibited better anti-erosion properties. Xu et al. (2022) explored the effect of gravity on ball valve's wear by the numerical simulations and experiments and reported that the plate surface wear first increased but then decreased along the centerline. Ma et al. (2020) examined the square gate valve's wear mechanism under gas–solid flow conditions. Their results revealed that the groove structure emerged as a determinant factor in wear distribution. Qian et al. (2023) explored the effect of tolerance parameters and spool blockage on the hydraulic valve flow. The results demonstrated a peak adhesive force at the particle diameter of 12 μm. Ou et al. (2022) examined the erosion wear of multistage regulating valves and reported that the cylinders, flat surfaces, and bevels of valves are susceptible to erosion. Jin et al. (2024b) studied how particle sphericity altered wear patterns in blackwater angle valves and reported that spherical particles have the greatest influence on erosion. Numerous researchers have explored control valve erosion under multiphase flow conditions, and the effect of vortex cores on particle trajectories and erosion remain unclear because of the concurrent influence of multiple variables.

Li et al. (2022) investigated wear and erosion during the opening/closing cycles of hydraulic spool valves. The erosive wear characteristics of hydraulic spool valves were found to be dependent on valve opening degrees by Yin et al. (2017). The numerical results revealed that the worn profile becomes more evenly distributed when the valve opening is small. A novel model was proposed to predict the wear profile by Li et al. (2024). The predicted results revealed that the relative error was no more than 2.25% compared with the experimental measurements. The erosion properties of centerline butterfly valves were examined by Liu et al. (2024b) under different valve opening and particle diameter condition. They discovered that as the valve's opening degree rises, so does erosion's severity. In the study of ball valve sealing surface erosion, Peng et al. (2021) discovered a stagnation zone in the sample's center. Liu et al. (2017) identified the failure characteristics of centerline butterfly valves and reported that as the pressure, mass flow, and maximum velocity rise, the valve's wear intensifies. In these works, the erosion wear characteristics of pipelines, hydraulic spool valves, ball valves, and centerline butterfly valves were investigated. More recently, more attention has been given to the hydraulic characteristics of this valve, which has an asymmetrical structure and three eccentric angles. The connection between the erosion rate and flow characteristics, including vorticity, particle trajectories, turbulence kinetic energy, and velocity, requires further in-depth exploration for tri-eccentric butterfly valves. Few studies have examined how vorticity influences erosion or how vortex core regions affect particle trajectories. Moreover, because valve damage typically starts at the sealing interface, the particle wear characteristics in this region need to be further investigated qualitatively.

An E/CRC-based erosion model is constructed to study the wear behaviour under sharp sand particle conditions. The particle shape, wall roughness, particle size distribution, and two-way coupling phase interaction are considered in the proposed erosion model. The dependence of erosion rates on the valve opening state is investigated. Correlation coefficients quantify the relationship between wall erosion and key flow parameters like vorticity and velocity. This work examines the association between the wear and flow parameters, particularly turbulence kinetic energy and particle trajectories, and analyzes the effect of vortex core regions on particle trajectories.

2. COMPUTATIONAL METHODS

2.1 Model of Geometry Representation and Discrete System

Figure 1 shows the valve's different parts and surfaces. With a nominal diameter of 400 mm, the valve is divided into 4 parts and 4 sections to investigate the erosion wear characteristics. Figure 2 shows the computational grid for fluid domain. The fluid domains extend 5D upstream and 10D downstream from the valve. The prefix 5D signifies a geometric extension of the nominal diameter by a factor of five. The channel length was proven to be sufficient for simulating turbulent flow (Geng et al., 2021). To improve the numerical stability and reduce skewness, the numerical model uses polyhedral meshes. To capture the flow details, further mesh refinement is applied to specific positions, including the press ring and valve stem.

2.2 Liquid-Phase Equation

The erosion wear behaviour of this valve is investigated under sand particle flow conditions. The fluid mass conservation is governed by the following equation:

$$\frac{\partial \rho}{\partial t}+\frac{\partial(\rho v_j)}{\partial x_j}=0 \tag{1}$$

The liquid density is represented by ρ, and v_j and x_j represents the j-directional velocity and displacement components.

To address turbulence, the realizable k–ε turbulence model is employed, whose effectiveness for control valve simulations has been well validated. (Shin et al., 1995; Zhao et al., 2022; Yang et al., 2024). Conservation equations for turbulent kinetic (k) and its dissipation rate (ε) take the following form:

$$\frac{\partial}{\partial t}(\rho k)+\frac{\partial}{\partial x_j}(\rho k u_j)=\frac{\partial}{\partial x_j}\left[\left(\mu+\frac{\mu_t}{\sigma_k}\right)\frac{\partial k}{\partial x_j}\right]+G_k-\rho\varepsilon \tag{2}$$

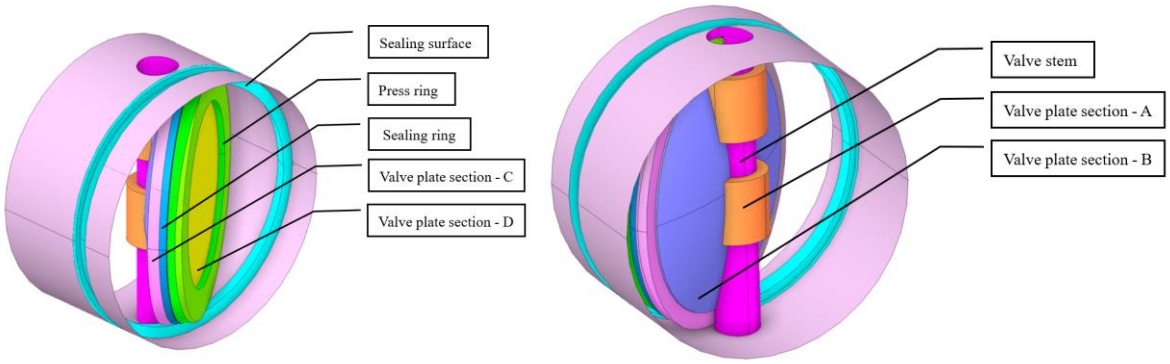

Fig. 1 Different parts and surfaces of the valve design

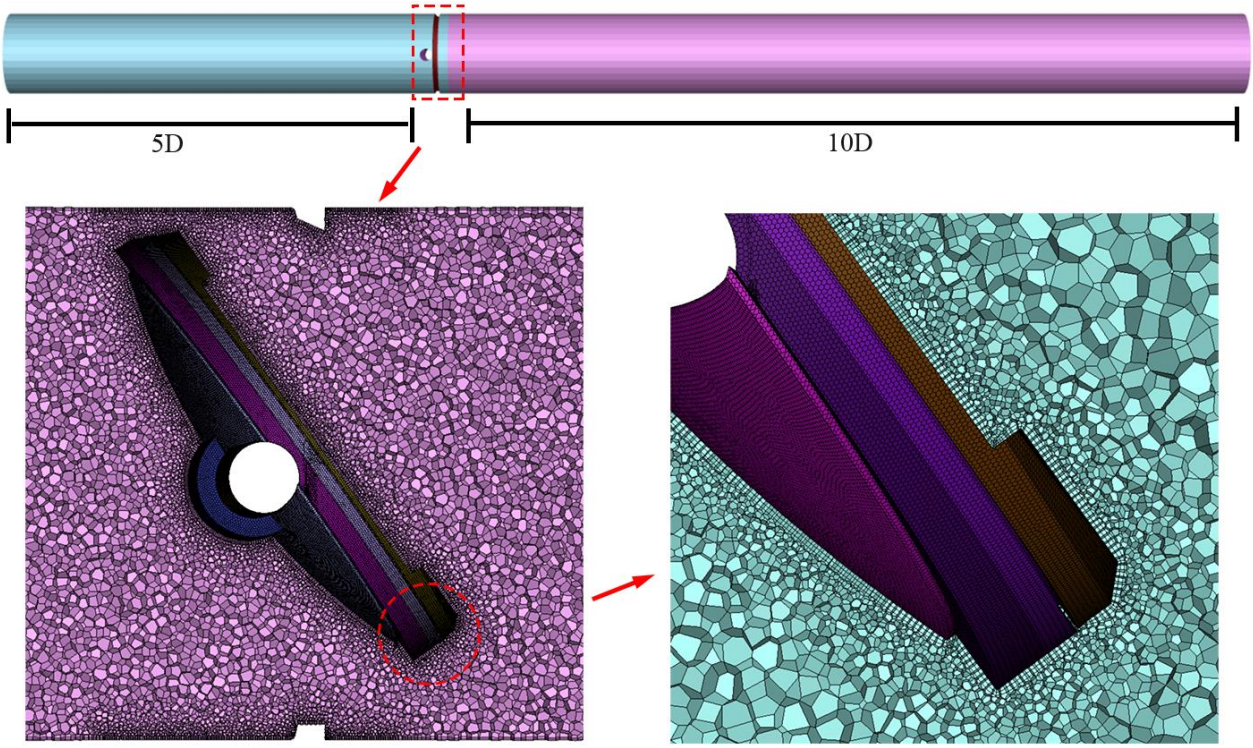

Fig. 2 Fluid domain grid of the pipeline and valve

$$\frac{\partial}{\partial t}(\rho\varepsilon)+\frac{\partial}{\partial x_j}(\rho\varepsilon u_j)=\frac{\partial}{\partial x_j}\left[\left(\mu+\frac{\mu_t}{\sigma_\varepsilon}\right)\frac{\partial\varepsilon}{\partial x_j}\right]+\rho C_1 S\varepsilon -\rho C_2\frac{\varepsilon^2}{k+\sqrt{\nu\varepsilon}} \tag{3}$$

$$C_1=\max\left[0.43,\frac{\eta}{\eta+5}\right],\eta=S\frac{k}{\varepsilon},S=\sqrt{2S_{ij}S_{ij}} \tag{4}$$

where ρ refers to the liquid density, u_j represents the j-direction time-averaged velocity, G_k the turbulence kinetic energy production from velocity gradients, and μ represents liquid viscosity. The other parameters include: turbulent viscosity μ_t, strain rate S_{ij}, turbulent Prandtl numbers σ_k and σ_ε, and constant C_2.

2.3 Particle Motion Model

Adopting a Lagrangian approach, the particles motion is described by:

$$m_p\frac{d\boldsymbol{u}_p}{dt}=m_p\frac{\boldsymbol{u}-\boldsymbol{u}_p}{\tau_r}+m_p\frac{\boldsymbol{g}(\rho_p-\rho)}{\rho_p}+\boldsymbol{F} \tag{5}$$

where m_p denotes particle mass, ρ_p and ρ correspond to the particle and liquid densities, $\boldsymbol{u}$ and $\boldsymbol{u}_p$ represent the liquid and particle velocities, $\boldsymbol{g}$ accounts for gravitational effect, $\boldsymbol{F}$ represents other external forces, and τ_r quantifies particle response characteristics. The particle relaxation time is calculated via (Gosman & Ioannides, 1983):

$$\tau_r=\frac{\rho_p d_p^2}{18\mu}\frac{24}{C_d Re} \tag{6}$$

where liquid viscosity, particle size, resistance coefficient, and relative Reynolds number are represented by μ, d_p, C_d, and Re, respectively. This dimensionless number can be formulated as:

$$Re = \frac{\rho d_p \left| \boldsymbol{u}_p - \boldsymbol{u} \right|}{\mu} \tag{7}$$

The shape of the sand particles is typically not spherical. It is assumed that the shape of the sand is irregular and that the surface is sharp in the numerical model. Regarding nonspherical particles, the drag coefficient expression is (Haider & Levenspiel 1989):

$$C_d = \frac{24}{Re_{sph}}(1 + b_1 Re_{sph}^{b_2}) + \frac{b_3 Re_{sph}}{b_4 + Re_{sph}} \tag{8}$$

where Re_{sph} is sphere Reynolds number. Parameters b_1 trough b_4 are model constants. The additional forces are those due to the virtual mass $\boldsymbol{F}_{vm}$ and pressure gradient $\boldsymbol{F}_{pg}$, as shown in Eqs. (9) and (10). Accounting for fluid acceleration effects, the virtual mass force takes the form:

$$\boldsymbol{F}_{vm} = C_{vm} m_p \frac{\rho}{\rho_p} \left(\boldsymbol{u}_p \nabla \boldsymbol{u} - \frac{d\boldsymbol{u}_p}{dt} \right) \tag{9}$$

where C_{vm} characterizes virtual mass effects, and the force arising from fluid pressure gradients takes the from:

$$\boldsymbol{F}_{pg} = m_p \frac{\rho}{\rho_p} \boldsymbol{u} \nabla \boldsymbol{u} \tag{10}$$

ANSYS recommends considering virtual mass and pressure gradient forces in particle modelling when $\rho/\rho_p > 0.1$. The Saffman lift is a lateral force that acts on a particle in a viscous fluid with a velocity gradient. Its mechanism arises from the asymmetric velocity field around the particle due to shear. The Saffman lift is based on the assumptions of low Reynolds numbers and weak shear and is generally not considered for high Reynolds numbers or larger particles where inertial effects dominate. Saffman and Magnus lift forces are neglected because of the large Reynolds numbers and particle diameter. The Rosin–Rammler formulation describes the particle size distribution in terms of the mass fraction of grains whose diameter exceeds d:

$$Y_d = e^{-(d/\bar{d})^n} \tag{11}$$

where Y_d represents the mass concentration at particle size d, the mean diameter is given by $\bar{d}$ and n controls the decay rate of the distribution.

2.4 Erosion Model

The E/CRC model serves as the basis for predicting sand-induced erosion. The erosion ratio can be written in the following form (Zhang et al., 2007a):

$$ER = C(\mathrm{BH})^{-0.59} F_s u_p^n f(\phi) \tag{12}$$

$$f(\phi) = \sum_{i=1}^{5} R_i \phi^i \tag{13}$$

ER quantifies wall material mass loss per unit mass, while BH denotes the Brinell hardness. F_s represents the particle shape coefficient: 0.2 for spherical, 0.53 for semispherical particles, and 1.0 for sharp-edged particles (Zhang et al., 2007, Li et al., 2022), and u_p denotes impact velocity. The model adopts empirical coefficients, where n takes a value of 2.41 and C is 2.17×10^{-7}. $f(\phi)$ denotes the function describing the impact angle ϕ (rad), where R_i (i=1,2,⋯,5) denote polynomial coefficients with values 5.3983, -10.1068, 10.9327, -6.3283, 1.4234 for R_1 through R_5, respectively.

The recovery coefficients can be expressed as (Forder et al., 1998):

$$e_n = 0.988 - 0.78\phi + 0.19\phi^2 - 0.024\phi^3 + 0.027\phi^4 \tag{14}$$

$$e_t = 1 - 0.78\phi + 0.84\phi^2 - 0.21\phi^3 + 0.028\phi^4 - 0.022\phi^5 \tag{15}$$

where e_n (normal) and e_t (tangential) are restitution coefficients.

3. CALCULATION VERIFICATION

3.1 Validation of the Flow Coefficients and Wear Model

Model accuracy was evaluated by comparing flow coefficients against experimental data across all valve openings. Detailed boundary conditions were reported previously (Yang et al., 2024). The flow coefficient (K_v) is defined as:

$$K_v = 10Q\sqrt{\frac{\rho}{\Delta P \rho_0}} \tag{16}$$

The volume flow rate Q with units of m^3/h, the pressure drop ΔP in kPa, and water density expressed in kg/m^3, and ρ_0 represents the density of water at 15 °C.

The water temperature during experimental testing was maintained at 15 °C, with deviations limited to ≤5% of the setpoint. During experimental testing, the pressure difference across the butterfly valve must be maintained at 100 kPa to ensure fully developed turbulent flow conditions within the pipeline. At each valve opening condition, experimental data are recorded after ensuring steady-state flow within the pipeline. Three consecutive experimental trials were conducted under identical conditions, with the maximum error over all the trials confirmed to remain below 5%. Fig. 3 presents the comparison between simulated and experimental flow coefficients, revealing strong consistency.

The E/CRC model (Zeng et al., 2014) is adopted for comparison with experimental data from a carbon steel elbow to verify the accuracy. The erosion experiment employed a 1.5D bend pipe (D = 50 mm) under a water flow at 4 m/s, with 400~500 μm sand particles at 0.235 kg/s mass flow rate. Fig. 4 compares erosion simulation results with experiment data, demonstrating the superior accuracy of the E/CRC over the Oka and Finnie formulations (Oka & Yoshida, 2005). Unlike both the Finnie and Oka models, the E/CRC approach incorporates particle shape and modifies the impact angle function.

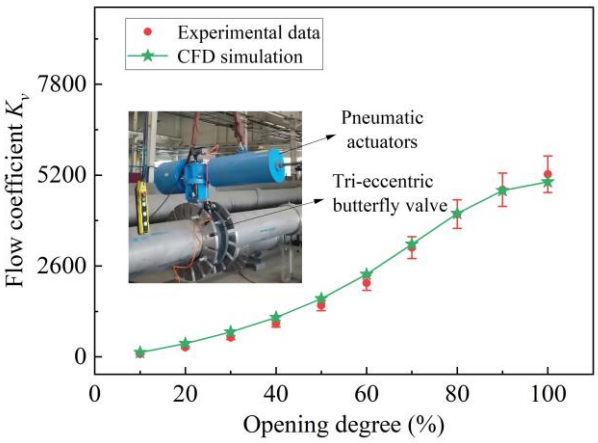

Fig. 3 Comparison of the numerical results of the flow coefficients and experimental results

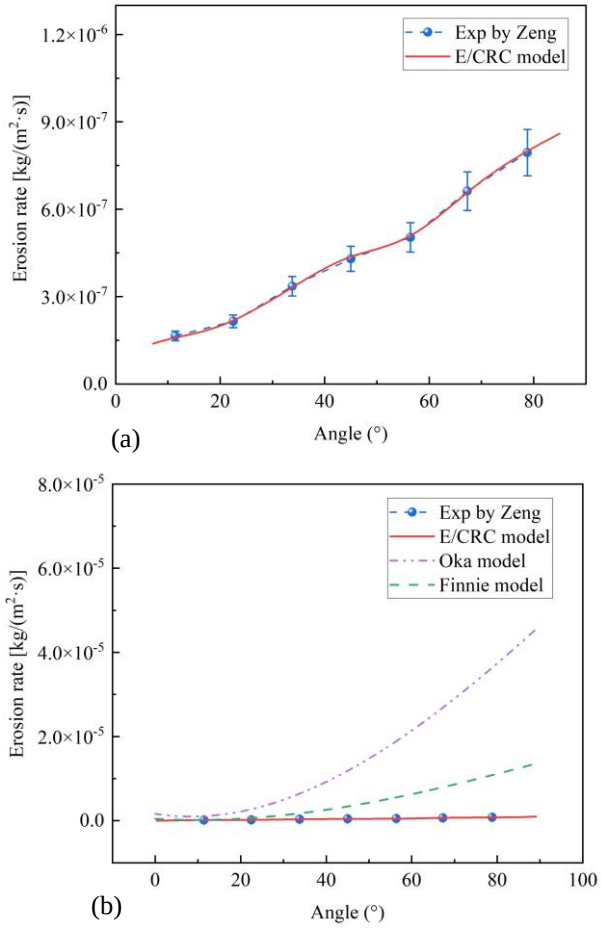

Fig. 4 Comparison of erosion simulation results and experiments. (a) E/CRC model and experiments, (b) other models and experiments

Figs. 3(a) and (b) show that the E/CRC better simulates sand-induced erosion on carbon steel.

3.2 Grid Independence and Boundary Conditions

Figure 5 shows how grid count affects sealing surface erosion, with stabilization occurring above 2.3 million grids. Thus, the simulation adopts meshing

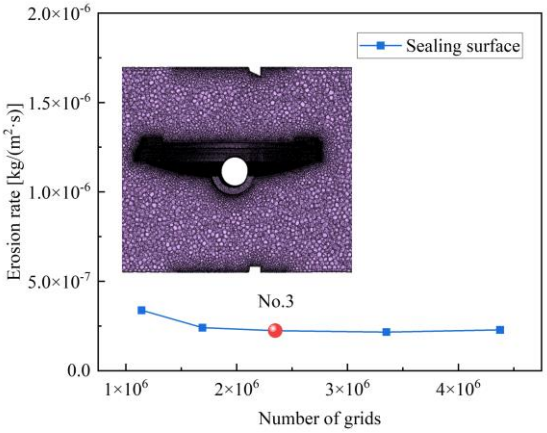

Fig. 5 Effect of the number of grids on the sealing surface's erosion rate

Table 1 Parameter settings of the discrete phase

Injection settings	**Parameters**
Injection type	Surface
Injection direction	Face normal direction
Phase interaction	Two-way coupling
Inlet total pressure	202650 Pa
Outlet static pressure	101325 Pa
Gravitational acceleration	9.8 m/s^2
Discrete phase boundary condition (Inlet/outlet)	Escape
Discrete phase boundary condition (wall)	Reflect
Erosion particle properties	**Properties**
Particle materials	Sand
Density	2650 kg/m^3
Injection velocity	4 m/s
Diameter	200-300 μm
Shape	1 (nonspherical)
Mass flow rate	0.235 kg/s
Wall surface settings	**Properties**
Material	Carbon steel
Brinell's hardness	183.5 kgf/mm^2 (Wen et al., 2024b)
Roughness constant	0.5
Roughness height	0.5 mm
Shear condition	No slip
Density	7850 kg/m^3

configuration No. 3, with 2 mm cells for all structural parts and 1 mm cells for the discrete boundary layers.

The standard wall function (Hong et al., 2023) is used because of the high Reynolds number. The ANSYS help document mentions that the Y^+ value of the first cell is not less than 20. The Y^+ values of the first cells of the wall surfaces are basically within the range of 20~300. The coupled approach is utilized for pressure–velocity coupling. The turbulence intensity calculated by the Reynolds number is set as 3%. All variables (momentum, pressure, etc.) are spatially discretized by a second-order upwind scheme. Table 1 provides details of the injection

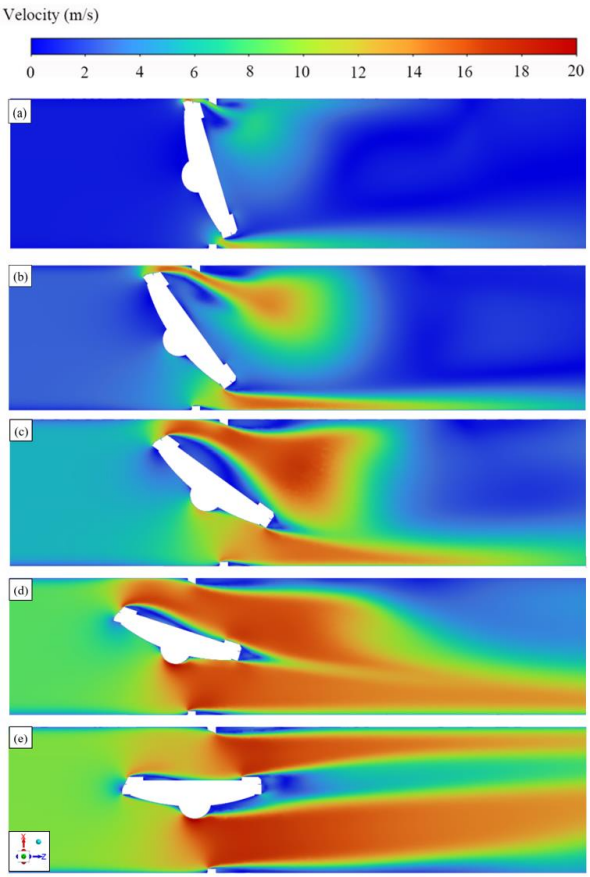

Fig. 6 2D velocity distribution at various valve opening degrees. (a) 20%, (b) 40%, (c) 60%, (d) 80%, (e) 100%

conditions, erosion particle attributes, and surface characteristics of the wall for the discrete phase.

4. RESULTS AND DISCUSSION

4.1 Solid-Liquid Flow

The 2D velocity distributions for all valve openings are visualized in Fig. 6. Figures 6(a) and (b) depict high-speed jets forming in the valve-seal interface clearance at 20% and 40% opening, respectively. The jet causes sealing surface erosion under small-opening conditions. Fig. 6 shows that as the valve opening increases, the flow channel's average velocity increases.

Figure 7 presents the 3D vector field at multiple valve opening degrees. The surface flow velocities of the valve stem and valve plate section A rise progressively as flow area expands. Larger valve openings lead to progressively higher surface flow velocities in the valve stem and plate section A. Figure 8 shows the 2D pressure distributions at various openings. As evidenced in Figs. 6 and 8, increasing valve opening elevates the pipeline's average fluid velocity progressively but reduces upstream static pressure, with inlet total and outlet static pressures held constant. Figure 9 displays the 3D pressure distributions at various openings, with a notable pressure drop across the upstream and downstream valve positions in subfigures (e) and (f). Figure 10 shows the 2D turbulent kinetic energy distributions. The constricted valve-seal clearance at 20% opening induces high turbulent energy (Fig. 10(a)). High turbulent kinetic energy may cause severe erosion of the surrounding wall.

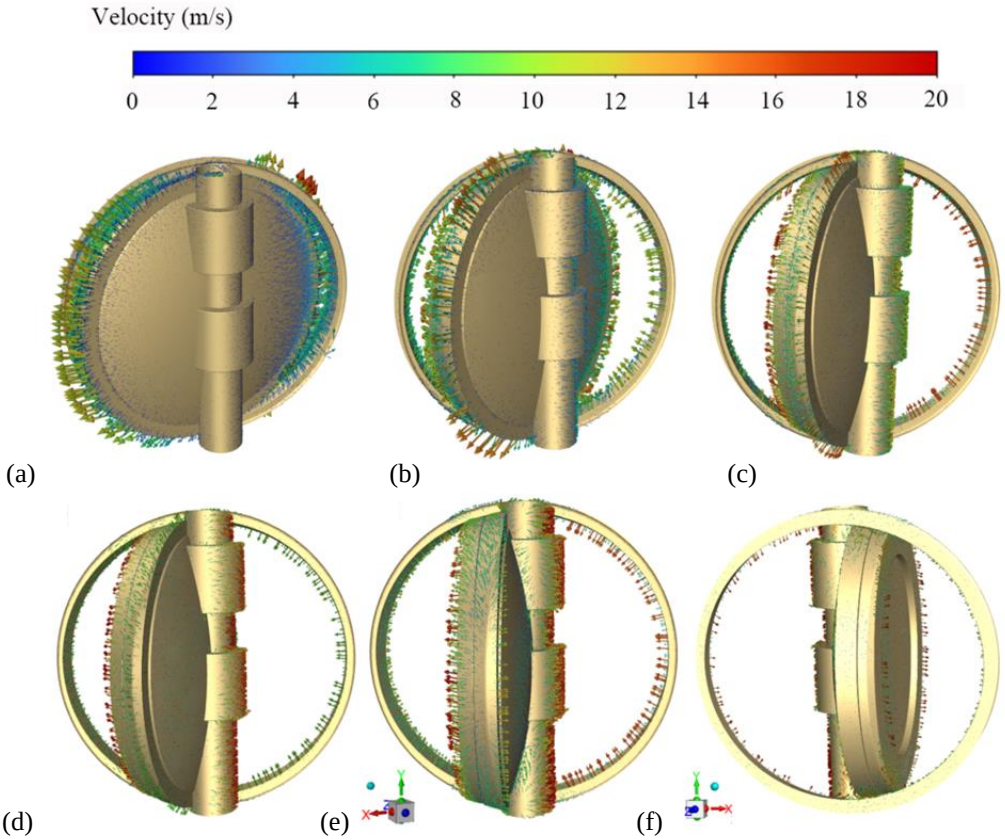

Fig. 7 3D vector distributions of the velocity at different valve opening degrees. (a) 20%, (b) 40%, (c) 60%, (d) 80%, (e) 100%, (f) 100% (another perspective)

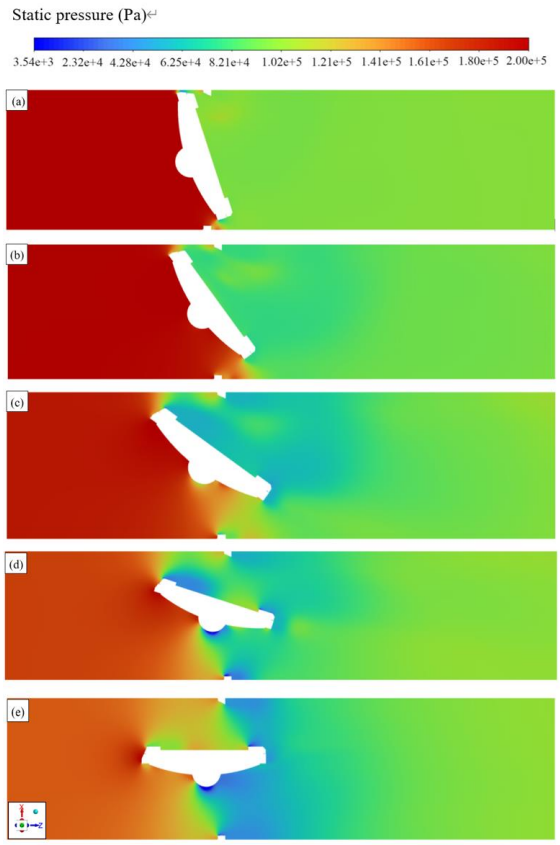

Fig. 8 2D pressure distributions at various opening degrees. (a) 20%, (b) 40%, (c) 60%, (d) 80%, (e) 100%

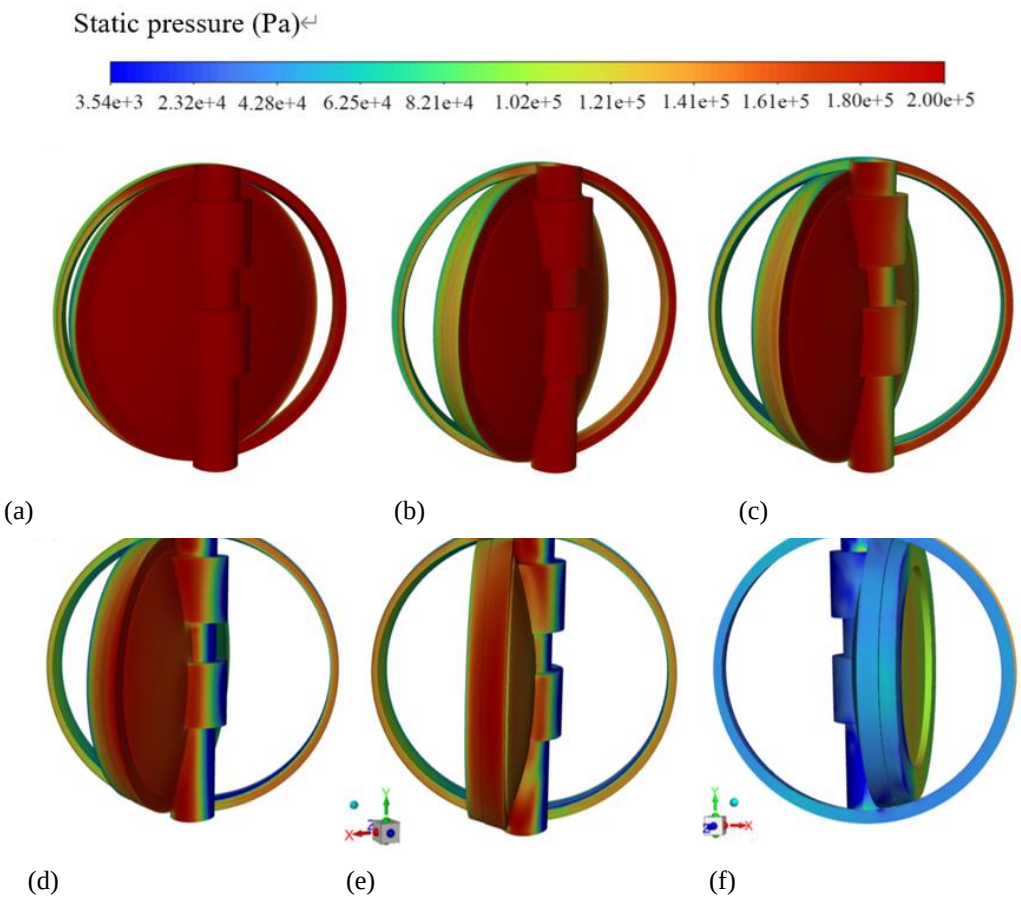

Fig. 9 3D pressure distributions at various opening degrees. (a) 20%, (b) 40%, (c) 60%, (d) 80%, (e) 100%, (f) 100% (another perspective)

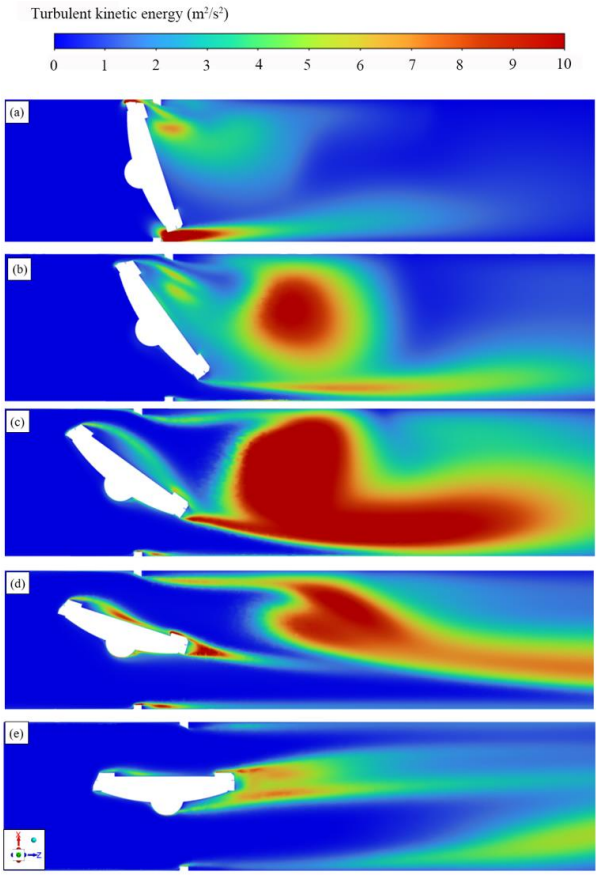

Fig. 10 2D turbulent kinetic energy distributions at various opening degrees. (a) 20%, (b) 40%, (c) 60%, (d) 80%, (e) 100%

4.2 Erosion Rate of Each Section

To study sand particle erosion of different parts, the valve is divided into 4 parts and 4 sections. Figure 11 presents the variation of average erosion rate with opening degree. Figure 11(a) demonstrates a gradual decline in the sealing surface's average erosion rate with increasing valve opening. Average sealing surface erosion varies between 2.24×10^{-7} and 8.53×10^{-7} kg/(m^2·s) with valve opening. With erosion rates elsewhere generally below 1×10^{-7} kg/(m^2·s), the sealing surface is the most susceptible to particle erosion wear. Figure 12 shows the erosion contours at various valve openings. Figures 11(d)-(f) and 12 demonstrate progressively rising erosion in the valve stem and plate sections A/B with increasing opening degree. Progressive velocity increases occur near the valve stem and plate sections A/B with enlarged openings. The velocity near the wall is an important factor leading to an increased erosion rate. Average erosion rates for all components (stem, plate Section A/B) range from 4.68×10^{-13} to 5.52×10^{-8} kg/(m^2·s). Figure 11(g) shows that the average erosion rate in plate Section C reaches the maximum value at 60% opening. High turbulent kinetic energy occurs near valve plate Section C (Fig. 10(c)), while the average erosion rate of Section D peaks at 40% opening (Fig. 11(h)). Figure 10(b) shows that high turbulent kinetic energy occurs near valve plate Section D. High velocity fluctuations (high turbulent kinetic energy) induce rotational movements, thereby enhancing the turbulent characteristics of the vortex (Zhang et al., 2024a). High-velocity fluctuations intensify erosion on Plate D with 40% valve opening. Section A/B erosion rates increase with valve opening, reaching maximum at 100%. By adjusting the valve opening, it is possible to reduce particle erosion in specific sections.

4.3 Erosion-Flow Characteristic Relationships

This study examines how flow characteristics (velocity, vorticity) influence erosion rate. Vorticity quantifies the rotational motion of fluid elements in a flow field. Vorticity can be written as:

$$\boldsymbol{\omega} = \nabla \times \boldsymbol{v} \tag{17}$$

where $\boldsymbol{\omega}$ and $\boldsymbol{v}$ represent the vorticity and velocity.

For 3D flow, the vorticity vector can be expressed as:

$$\boldsymbol{\omega} = \begin{pmatrix} \omega_x \\ \omega_y \\ \omega_z \end{pmatrix} = \begin{pmatrix} \dfrac{\partial w}{\partial y} - \dfrac{\partial v}{\partial z} \\ \dfrac{\partial u}{\partial z} - \dfrac{\partial w}{\partial x} \\ \dfrac{\partial v}{\partial x} - \dfrac{\partial u}{\partial y} \end{pmatrix} \tag{18}$$

The vorticity magnitude can be expressed as:

$$|\boldsymbol{\omega}| = \sqrt{\omega_x^{\,2} + \omega_y^{\,2} + \omega_z^{\,2}} \tag{19}$$

Figure 13 shows the average erosion rate and average vorticity magnitude of each part at different valve opening degrees. Below 80% opening, Fig. 13(a) reveals gradual declines in both the sealing surface's average erosion rate and vorticity magnitude. This finding reveals that the sealing surface's erosion rate correlates with its mean vorticity magnitude. Under constant inlet/outlet pressures, the sealing surface reaches maximum erosion rate (8.53×10^{-7} kg·m^{-2}·s^{-1}) and vorticity magnitude (4494.3 s^{-1}) at 20% valve opening. The sealing surface's erosion is 3.56×10^{-7} kg/(m^2·s) at an 80% opening degree, and the average vorticity magnitude of the sealing surface is 2896.6 s^{-1} at an 80% opening degree.

The average erosion rate of the sealing surface decreases by 58.3%, and the average vorticity magnitude of the sealing surface decreases by 35.5% as the valve opening rises from 20% to 80%. A high vorticity magnitude represents a stronger rotation effect of fluid on the wall. The sealing surface's average erosion rate gradually decreases with decreasing average vorticity magnitude on the sealing surface wall. Figure 13(b) demonstrates that below 80% valve opening, both the valve stem's average erosion rate and vorticity magnitude show progressive increases. Minimum values for the valve stem's average erosion rate (1.30×10^{-11} kg·m^{-2}·s^{-1}) and magnitude (408.7 s^{-1}) occur at 20% opening. Peak values for the valve stem's average erosion rate (5.20×10^{-8} kg·m^{-2}·s^{-1}) and vorticity (4565.3 s^{-1}) occur at 80% opening. A vortex represents a fluid region with concentrated vorticity, particularly exhibiting intense rotational motion in its core. High-vorticity regions can lead to the formation of vortices. When vorticity is concentrated in a specific area, it can lead to the formation of vortex structures. The

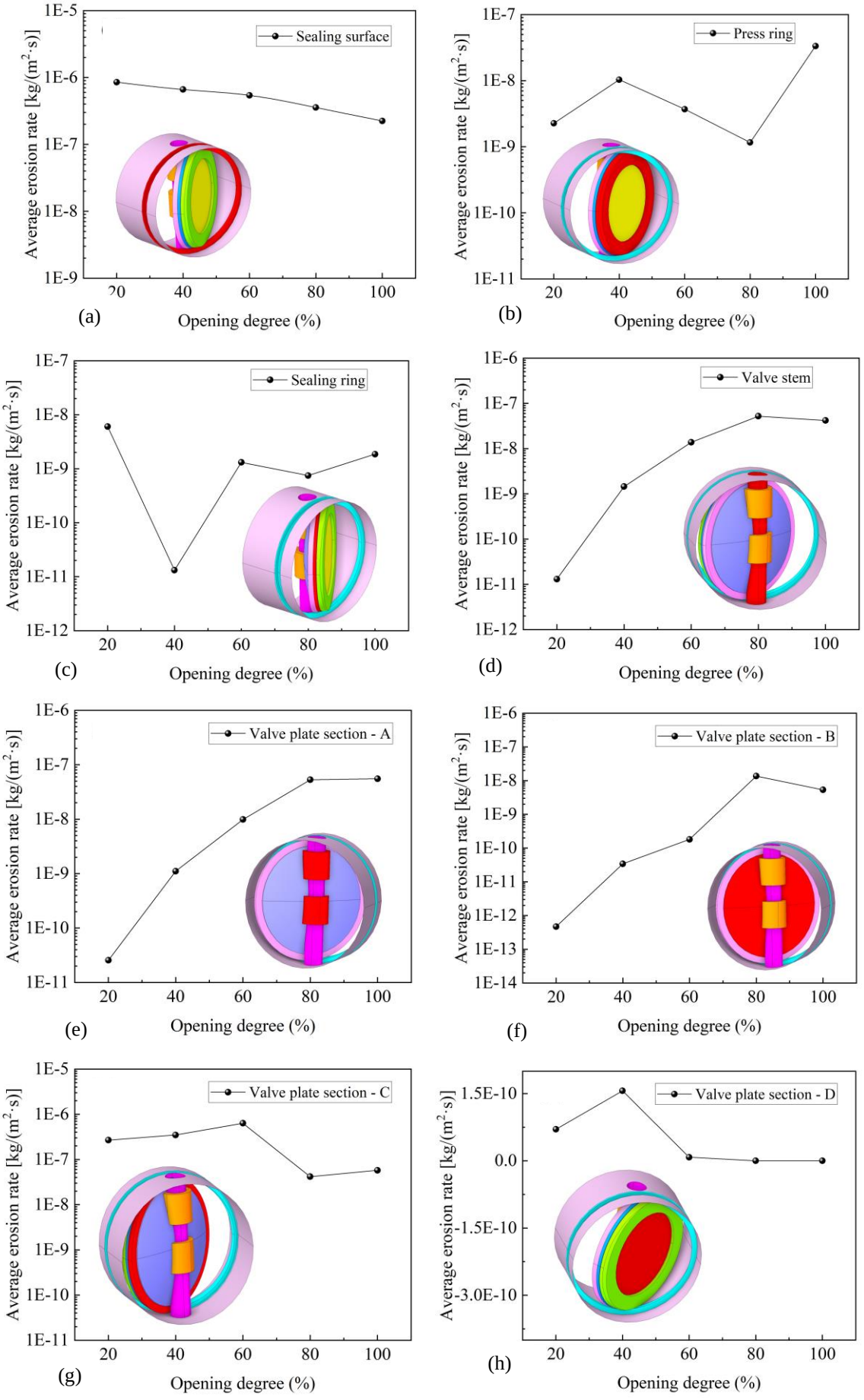

Fig. 11 Average erosion rate at different valve opening degrees. (a) Sealing surface, (b) press ring, (c) sealing ring, (d) valve stem, (e) valve plate Section A, (f) valve plate Section B, (g) valve plate Section C, (h) valve plate Section D

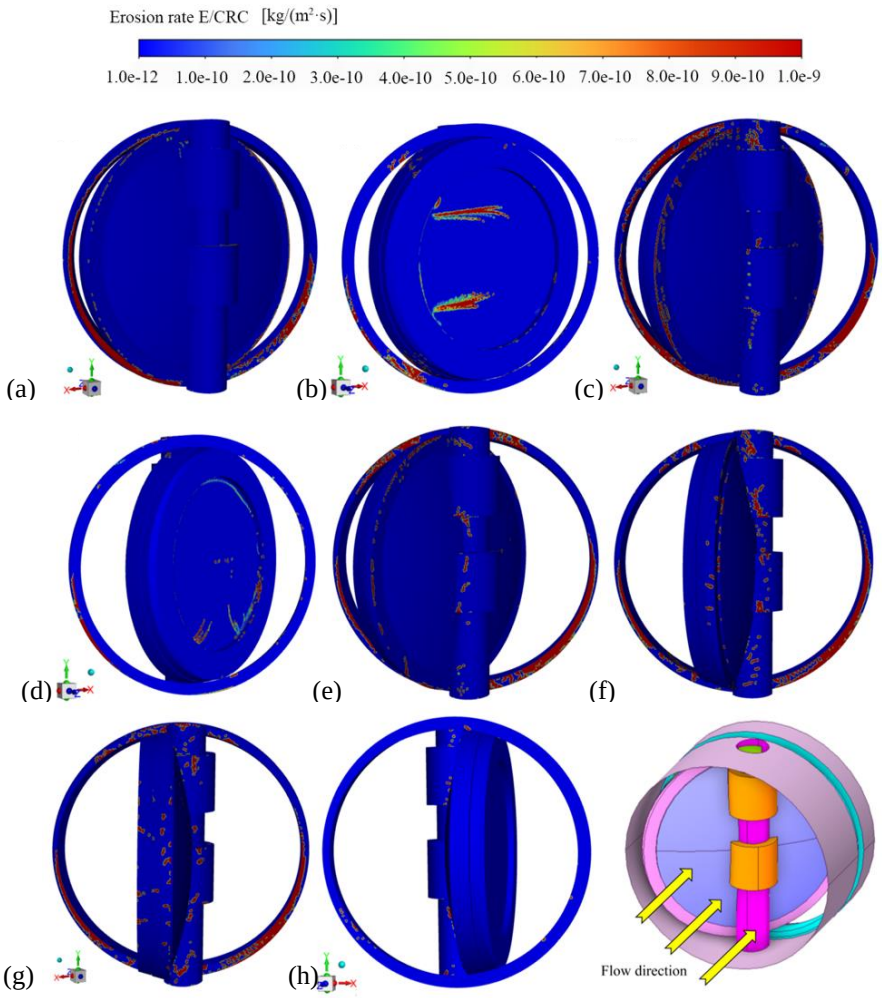

Fig. 12 Erosion contours at different valve opening degrees. (a) 20%, (b) 20% (another perspective), (c) 40%, (d) 40% (another perspective), (e) 60%, (f) 80%, (g) 100%, (h) 100% (another perspective)

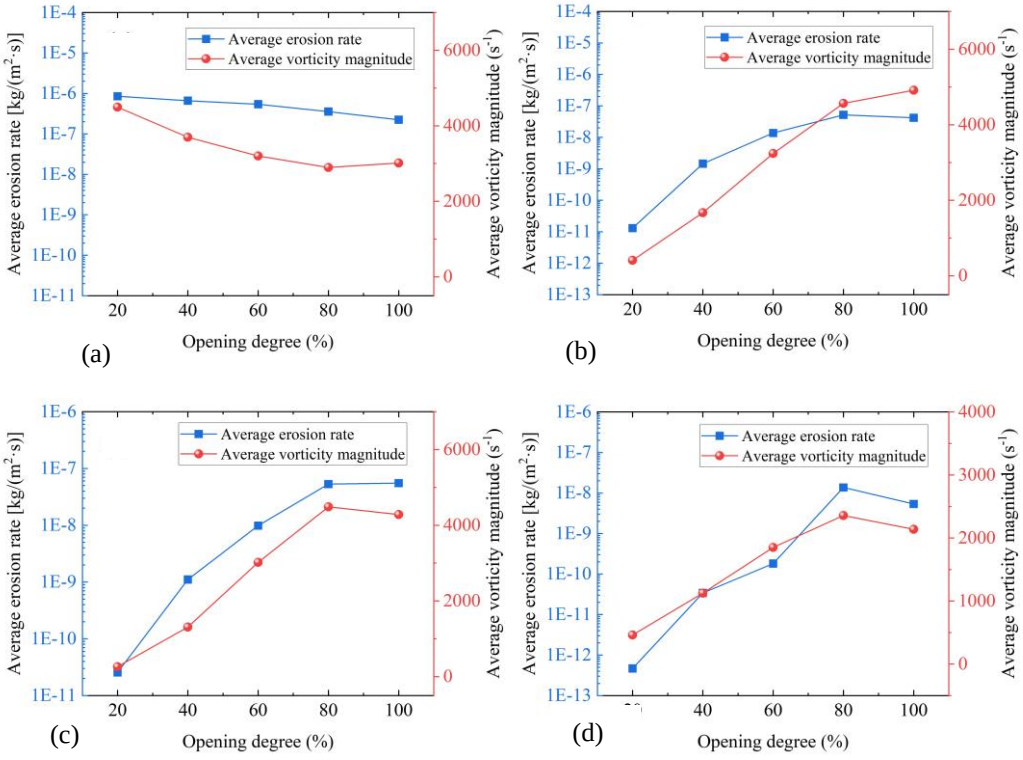

Fig. 13 Average erosion rate and average vorticity magnitude at different valve opening degrees. (a) Sealing surface, (b) valve stem, (c) valve plate Section A, (d) valve plate Section B

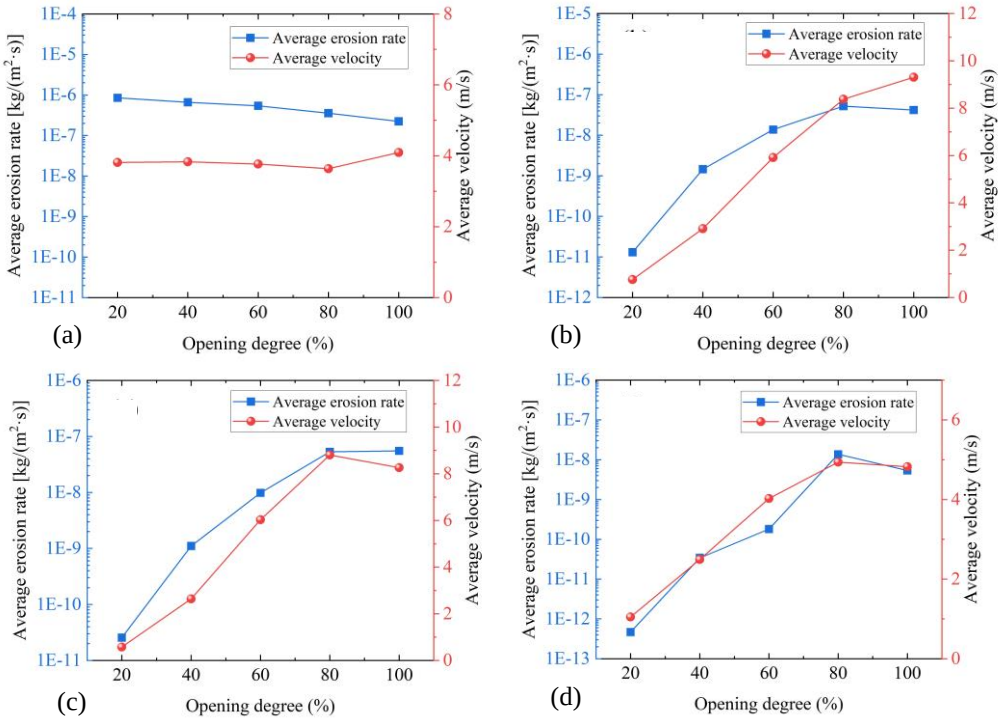

Fig. 14 Average erosion rate and average velocity at different valve opening degrees. (a) Sealing surface, (b) valve stem, (c) valve Plate A, (d) valve Plate B

increase in vorticity around the wall can generate vortex structures and increase the angular velocity of the sand particles, which consequently enhances wall erosion. With increasing valve opening, the average vorticity magnitude of the fluid around the wall of the valve stem increases, inducing enhanced erosion. The increase in the average vorticity magnitude around the walls of valve plate Sections A and B leads to an increased erosion rate of the walls, as evidenced in Figs. 13(c) and (d).

Tri-eccentric butterfly valve erosion correlates strongly with local vorticity magnitude, particularly at the sealing surface, stem, and plate. Figure 14 shows the average erosion rate and average velocity of each part at different valve opening degrees. Average velocities of the parts are the average velocities near the walls. Figure 14(a) demonstrates a 73.7% reduction in the sealing surface's average erosion rate, with a concurrent 7.3% increase in velocity, as the opening rises from 20% to 100%. Below 80% valve opening, Fig. 14(b) demonstrates progressive increases in both the stem's average erosion rate and flow velocity.

At 20% opening, the valve stem exhibits a minimum erosion rate of 1.30×10^{-11} kg/(m^2·s) and a minimum average velocity of 0.76 m/s. Under 80% opening, the valve stem exhibits its highest erosion rate (5.20×10^{-8} kg·m^{-2}·s^{-1}) and an average velocity of 8.4 m/s. A larger valve opening enhances the fluid's average along the stem wall, thereby accelerating erosion. The increase in the average velocity near valve plate Sections A and B can lead to an increased erosion rate of the walls, as evidenced in Figs. 14(c) and (d). Previous studies suggests that velocity not only directly influences sealing surface erosion but also modulates its effects through interactions with vorticity. Velocity critically affects erosion in tri-eccentric butterfly valves, particularly impacting sealing surfaces, stems, and plates. Using correlation coefficients, we examine how wall erosion associates with flow parameters including vorticity and velocity.

Table 2 Correlation coefficients r_{vo} and r_{ve}

Valve parts	r_{vo}	r_{ve}
Sealing surface	0.92	-0.33
Valve stem	0.92	0.92
Valve plate section - A	0.91	0.90
Valve plate section - B	0.73	0.69

We employ correlation coefficients (r) to analyze how erosion rates associate with flow parameters including vorticity and velocity.

$$r=\frac{\sum(x_i-\bar{x})(y_i-\bar{y})}{\sqrt{\sum(x_i-\bar{x})^2\sum(y_i-\bar{y})^2}} \tag{20}$$

where $\bar{x}$ and $\bar{y}$ represent sample averages, x_i and y_i (i=1,2,⋯,n) are two variables (erosion rate and vorticity or velocity). r_{vo} represents the vorticity-erosion correlation coefficient, and r_{ve} denotes velocity-erosion correlation coefficient. The correlation coefficients r_{vo} and r_{ve} are listed in Table 2, where valve stem r_{vo} is 0.92, indicating a strong correlation between the erosion rate and the average vorticity magnitude of the valve stem. The valve stem's r_{ve} value of 0.92 suggests a strong erosion rate-average velocity correlation. The erosion rate of the valve stem is affected by both velocity and vorticity. The r_{vo} value of the sealing surface is 0.92, and the r_{ve} value of the sealing surface is -0.33. This finding indicates that vorticity has a primary influence on sealing surface's erosion, whereas

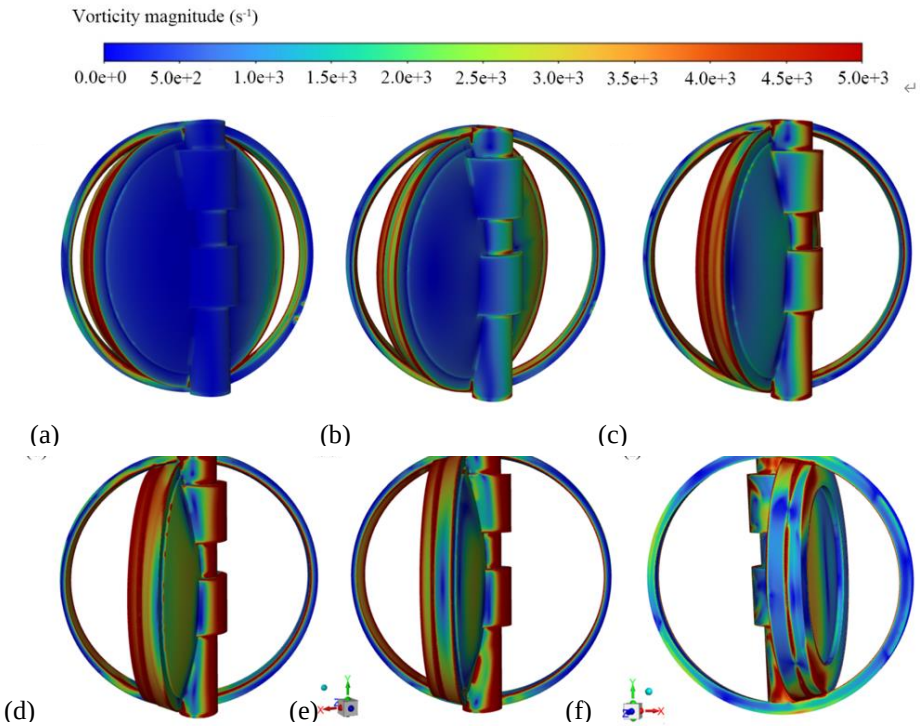

Fig. 15 Vorticity magnitude contours at different valve opening degrees. (a) 20%, (b) 40%, (c) 60%, (d) 80%, (e) 100%, (f) 100% (another perspective)

velocity exhibits only a minor effect under these boundary conditions.

The r_{vo} value of valve section Plate B is 0.73. This indicates a significant connection between the erosion rate and the average vorticity magnitude of valve plate Section B. The r_{ve} value of valve section Plate B is 0.69. These findings indicate a significant erosion-velocity connection in plate Section B. Figure 15 displays the vorticity magnitude distribution at varying valve openings. Figure 15 demonstrates how vorticity magnitudes of the valve stem and valve plate Section A gradually increase as the valve opening degree approaches 80%. Figure 15(a) shows that the sealing surface's vorticity magnitude exceeds those of the valve stem, valve plate Section A and valve plate Section B at a 20% valve opening degree. The vorticity distribution is significantly influenced by valve openings.

4.4 Relationship Between the Trajectory of the Particles and the Vortex Core Region

The trajectory of the particles can be influenced by the vortex core. To visualize this region, the *Q*-criterion technique is applied (Lin et al., 2021). The equation representing the characteristics of the velocity gradient tensor is given by (Hunt et al., 1988):

$$\lambda^3 + P\lambda^2 + Q\lambda + R = 0 \tag{21}$$

After defining the velocity gradient tensor invariants (*P*, *Q*, *R*), we present its two-component separation:

$$\nabla \boldsymbol{V} = \frac{1}{2}(\nabla \boldsymbol{V} + \nabla \boldsymbol{V}^{\mathrm{T}}) + \frac{1}{2}(\nabla \boldsymbol{V} - \nabla \boldsymbol{V}^{\mathrm{T}}) = \boldsymbol{A} + \boldsymbol{B} \tag{22}$$

The symmetric and antisymmetric parts of the velocity gradient tensor are represented by $\boldsymbol{A}$ and $\boldsymbol{B}$, respectively. The second invariant of this tensor is the *Q*-criterion.

$$Q = \frac{1}{2}(\|\boldsymbol{B}\|_F^2 - \|\boldsymbol{A}\|_F^2) \tag{23}$$

The symbol $\|\ \|_F$ refers to the Frobenius norm. The *Q*-criterion threshold affects vortex formation. Nevertheless, a definitive criterion to establish the threshold remains absent.

Figure 16 shows the velocity contours and particle tracks in the vortex core region at different valve opening degrees (from the front view). The bright magenta lines are used to trace the trajectory of the particles in Figs. 16 and 17. To visualize the important vortex structures, adjusting the actual value of *Q* at different degrees of valve opening is essential. Figure 17 shows the velocity contour and particle tracks in the vortex core region (from the side view). Figure 16(a) illustrates the occurrence of vortex separation on the downstream side at 20% valve opening. When the opening exceeds 40%, two tapered vortex structures are observed downstream, and the vortices appear to be approximately symmetrical, as shown in Figs. 16 and 17.

Figure 16 indicates that in regions upstream from the valve plate, the particle paths are consistent and unaffected by disturbances. Owing to the flow restriction of the valve plate, vortices are formed downstream. During the 80~100% opening, Figs. 16(d), (e), 17(d), and (e) show that the positions of the two vortices change significantly. The position of the vortices significantly influences the trajectory of the sand particles (Figs. 16 and 17). Owing to the formation of vortex cores, the trajectory of sand particles downstream becomes highly complex.

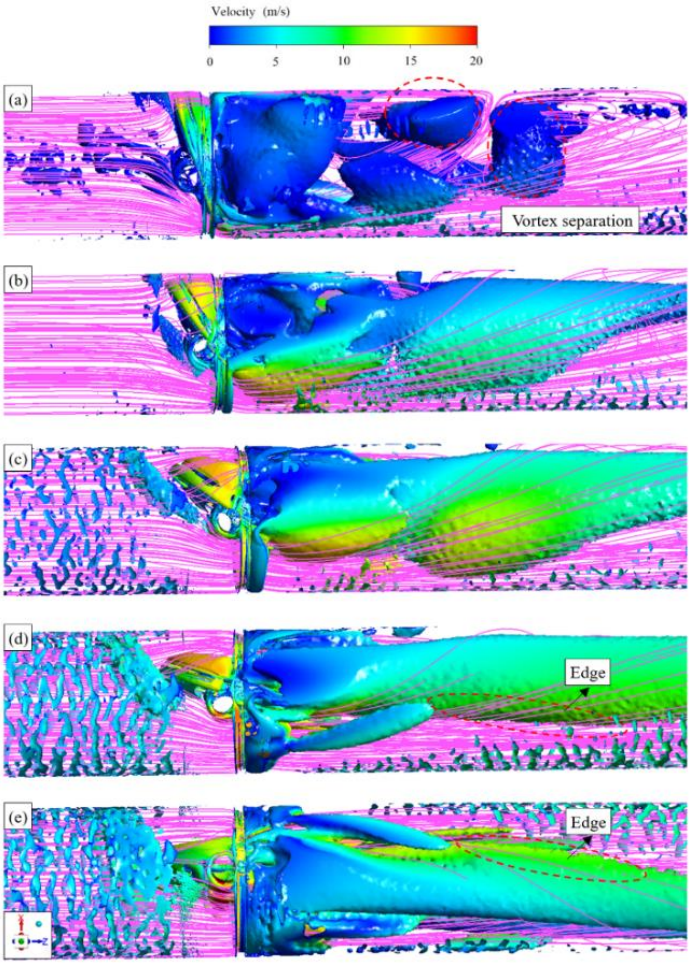

Fig. 16 Velocity contours and particle tracks in the vortex core region at different valve opening degrees (the front view). (a) 20% (Q=15 s^{-2}), (b) 40% (Q=100 s^{-2}), (c) 60% (Q=100 s^{-2}), (d) 80% (Q=100 s^{-2}), (e) 100% (Q=160 s^{-2})

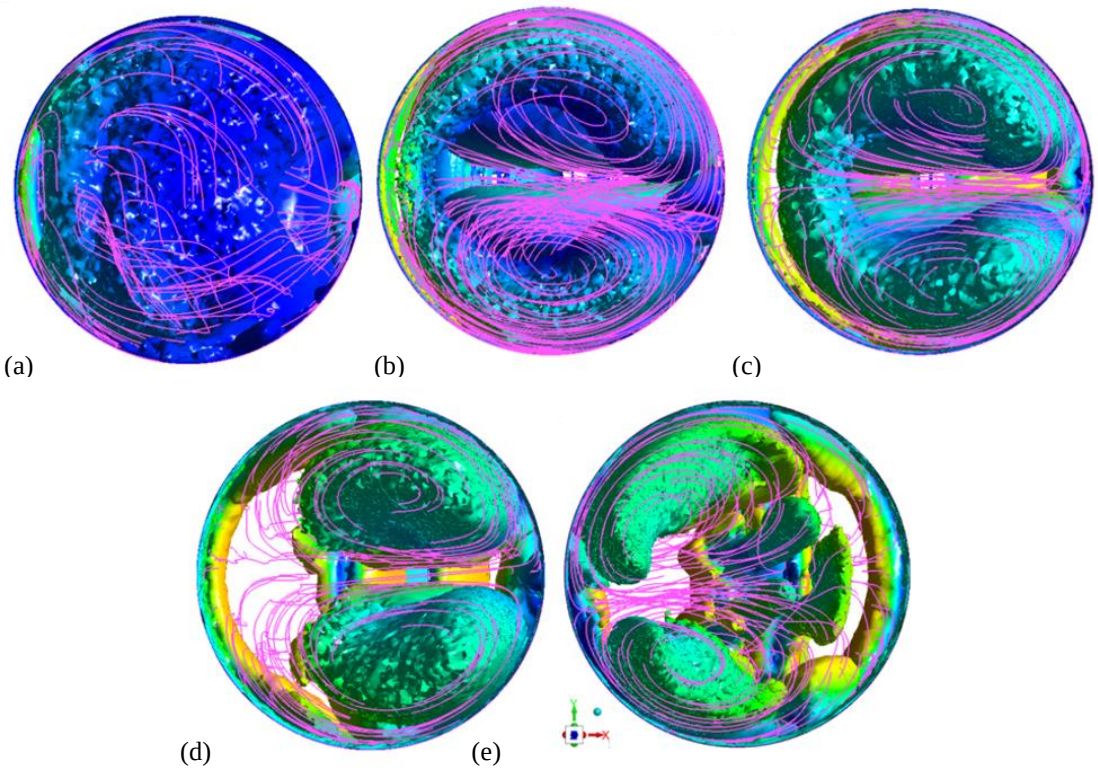

Fig. 17 Velocity contours and particle tracks in the vortex core region at different valve opening degrees (the side view). (a) 20% (Q=15 s^{-2}), (b) 40% (Q=100 s^{-2}), (c) 60% (Q=100 s^{-2}), (d) 80% (Q=100 s^{-2}), (e) 100% (Q=160 s^{-2})

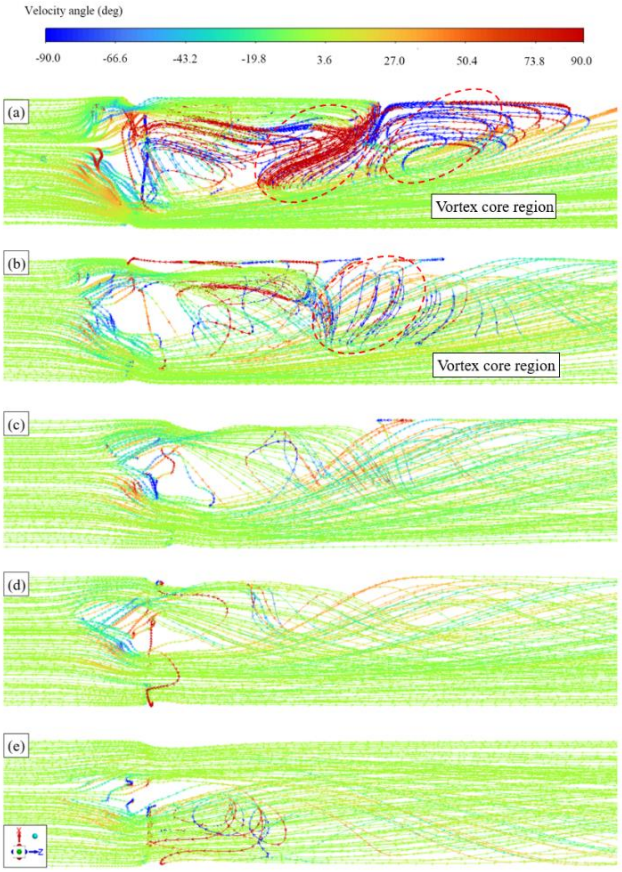

Fig. 18 Particle tracks with velocity angle distributions at different valve opening degrees. (a) 20%, (b) 40%, (c) 60%, (d) 80%, (e) 100%

Using velocity angle, we examine vortex core impacts on particle paths.

$$\alpha = \tan^{-1}\left(\frac{v_{tangential}}{v_{axial}}\right) \tag{24}$$

where α is the velocity angle, $v_{tangential}$ (tangential) and v_{axial} (axial) are velocities.

Figure 18 shows the particle tracks with velocity angle distributions. The velocity angle nears ±90° in the vortex core region under 20% or 40% valve opening, as visualized in Figs. 18(a) and (b). The velocity angle is close to 0° in the regions without vortices. This result indicates that the vortex core affects the particle trajectory by influencing the direction of the particle's movement at openings below 40%. The particles in the vortex core region exhibit strong clockwise or counterclockwise rotation. At 80% or 100% opening, the vortex core alters the particle velocity. Figure 16(d) and (e) demonstrate that at the edges of the tapered vortex structures, the particle flow velocity is increased, reaching approximately 12~16 m/s. The vortex core affects both the particle velocity and velocity angle, but the influence extent varies with the degree of opening.

Figures 19 and 20 show the turbulence kinetic energy contours of different cross-sections in the *z* direction and vortex core region at 80% and 100% valve opening degrees. Figure 21 shows the average turbulence kinetic energy of different cross-sections in the z direction at 80% and 100% opening degrees. Compared with the blue region, the red region is considered to have greater turbulence kinetic energy, as shown in Figs. 19 and 20.

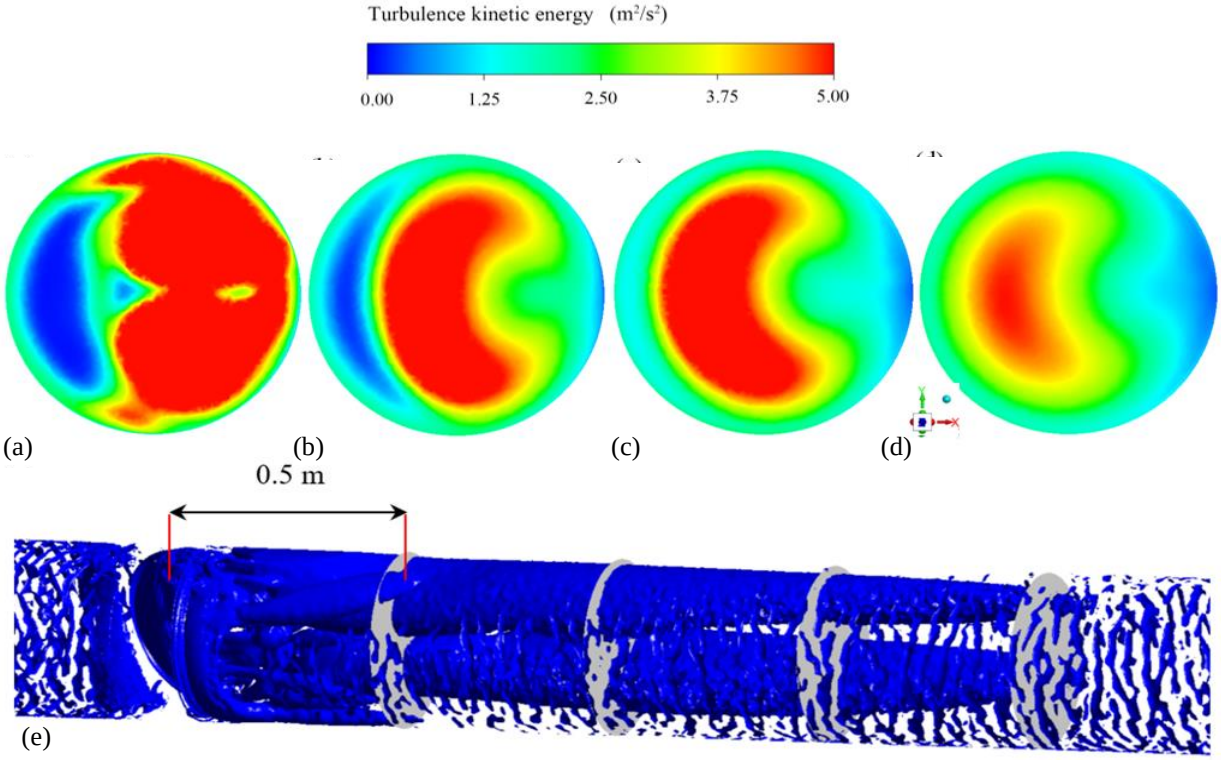

Fig. 19 Turbulence kinetic energy contours of different cross-sections in the *z* direction and vortex core region at an 80%valve opening degree. (a) *z*=0.5 m, (b) *z*=1.0 m, (c) *z*=1.5 m, (d) *z*=2.0 m, (e) vortex core region for *Q*=100 s^{-2}

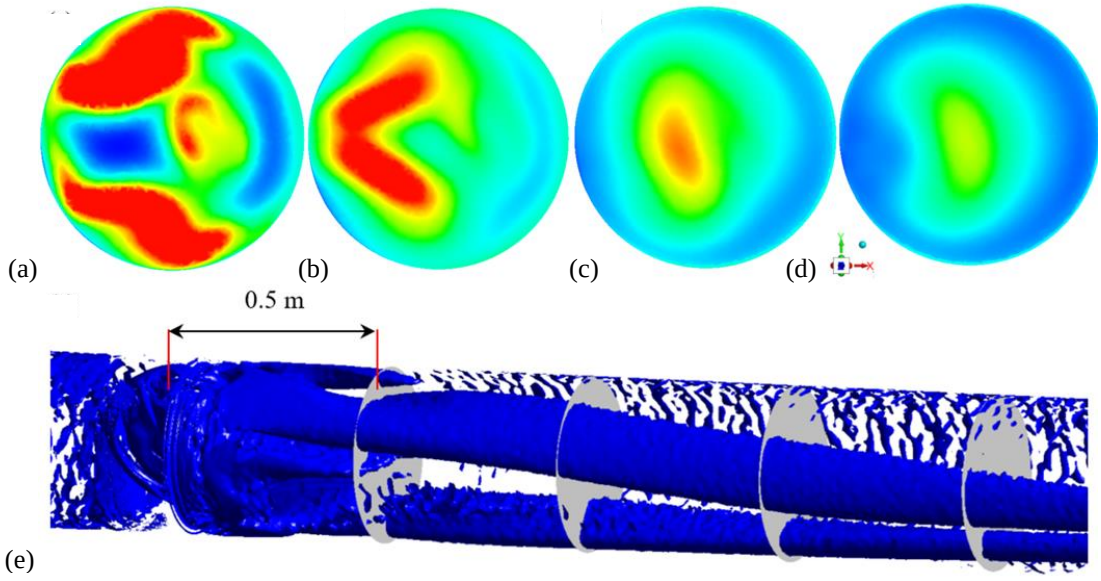

Fig. 20 Turbulence kinetic energy contours of different cross-sections in the *z* direction and vortex core region at a 100% valve opening degree. (a) *z*=0.5 m, (b) *z*=1.0 m, (c) *z*=1.5 m, (d) *z*=2.0 m, (e) vortex core region for *Q*=160 s^{-2}

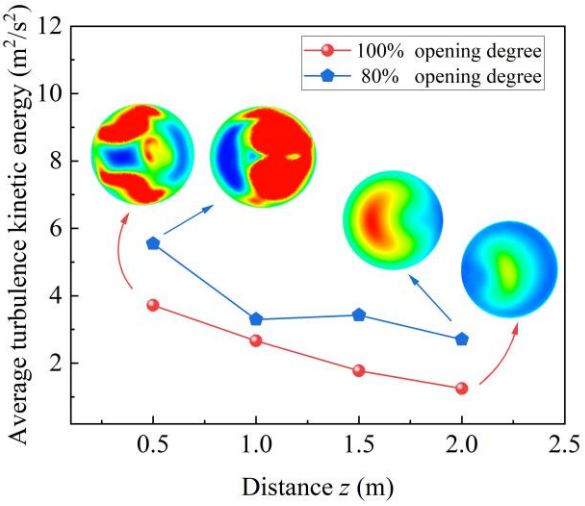

Fig. 21 Average turbulence kinetic energy of different cross-sections in the z direction at 80% and 100% valve opening degrees

A comparison of Figs. 19(a) and (e), as well as Fig. 20(a) and (e), reveals that the vortex core region highly overlaps with the region of high turbulence kinetic energy at 80% and 100% valve opening degrees when *z* is 0.5 m. Figure 21 shows that the average turbulence kinetic energy is 5.54 m^2/s^2 at an 80% valve opening degree at *z* = 0.5 m. The average turbulence kinetic energy of the cross section is 2.70 m^2/s^2 at an 80% valve opening when *z* is 2.0 m. The average turbulence kinetic energy of the cross-section decreases by 51.26% at an 80% valve opening degree when *z* changes from 0.5 to 2.0 m. Figures 19 and 20 show that the average turbulence kinetic energy of the cross-section gradually decreases at a 100% valve opening degree when *z* changes from 0.5 to 2.0 m. The average turbulence kinetic energy of the cross-section decreases by 66.40% at a 100% valve opening degree when *z* changes from 0.5 to 2.0 m. The average turbulence kinetic energy of the cross-section downstream generally tends to increase as the cross-section approaches the valve plate at 80% and 100% opening, respectively.

This phenomenon may lead to increased erosion and wear in areas closer to the valve plate downstream. The average turbulence kinetic energy of the cross-section decreases by 19.39% during opening progression from 80% to 100% when *z* is 1.0 m. Due to the increase in valve opening from 80% to 100%, the average turbulence kinetic energy of the cross-section decreases by 53.70% at *z* = 2.0 m. To reduce the average turbulent kinetic energy downstream, the valve opening can be adjusted.

4.5 Relationship Between the Particle Trajectory and Erosion Rate

Figure 22 shows that particle tracks of the particle velocities at various valve opening degrees. Figures 22(a) and (b) demonstrate that vortexes emerge downstream at 20% and 40% valve opening degrees. Figures 12(b) and (d) show that valve plate Section D has experienced erosion due to sand particles carried by vortices. The valve stem, valve plate Section A, and valve plate Section B upstream are subjected to both cutting and impact erosion at 20% and 40% openings. Figure 22(e) demonstrates that the material losses of the valve stem and valve plate Sections A and B primarily result from abrasive cutting at 100% opening. The valve plate Section C erosion reaches a maximum, as evidenced in Fig. 11(g). Erosion wear is influenced by a coupled interaction between impact angle and particle velocity. At a 20% valve opening degree, the impact angle between valve Plate C and the particle flow reaches its maximum value of approximately 80°, whereas the particle flow velocity around valve Plate C decreases to a minimum range of 8~10 m/s. At 100% opening, the impact angle between valve Plate C and the particle flow reaches its minimum value of approximately 0°, whereas the particle flow velocity around valve Plate C increases to a maximum range of 16~20 m/s.

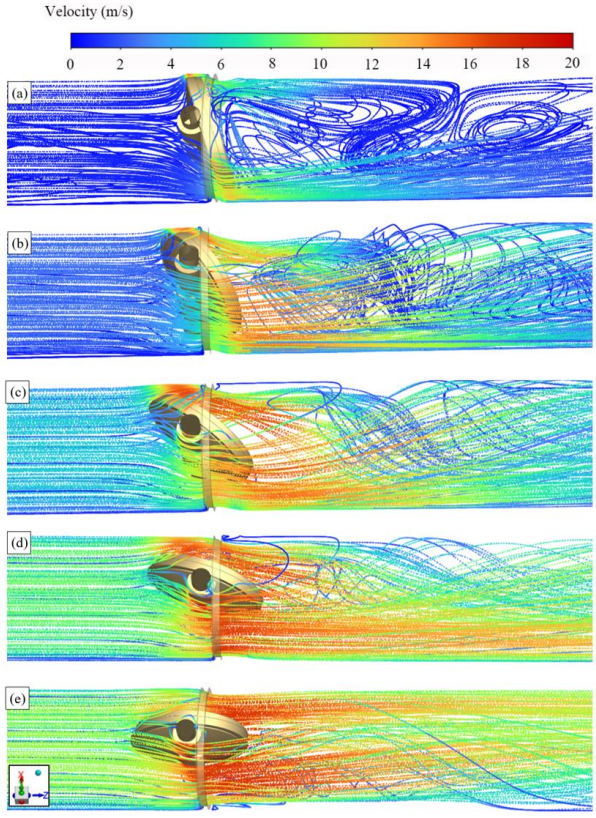

Fig. 22 Particle tracks of the particle velocities at different valve opening degrees. (a) 20%, (b) 40%, (c) 60%, (d) 80%, (e) 100%

Under 80% and 100% valve opening degrees, the erosion on partial regions of valve Plate C is mitigated because of the stem shielding. As the valve fully opens, sand particles induce cutting wear on the stem, plate Section A, and other components. Because the upstream flow channel's cross-sectional area exceeds that of the sealing surface, a vena contracta region forms when the fluid medium passes through the sealing surface. This causes a significant increase in the speed of the solid particles as the sand moves across the sealing surface, thereby accelerating the erosion of the surface.

5. CONCLUSION

A tri-eccentric butterfly valve erosion model based on E/CRC is developed. The particle shape, wall roughness, particle size distribution, and two-way coupling phase interaction are considered in the proposed erosion model. The valve opening's influence on erosion of each section is investigated. The correlation coefficient is used to reveal the association between erosion and flow characteristics. The conclusions are as follows:

1. As the valve opening degree increases, the sealing surface's wear gradually decreases. Seal face wear rate ranges from 2.24×10^{-7} to 8.53×10^{-7} kg/(m^2·s) at different valve opening degrees. The sealing surface typically experiences a higher erosion rate at all valve opening degrees than the other sections. Therefore, the sealing surface is the most susceptible to sand particle erosion.
2. The increase in vorticity around the wall can affect vortex formation and increase the angular velocity of sand particles, leading to an increased erosion rate of the walls. High velocity enhances the collision and cutting energy of sand particles, resulting in a faster rate of wall erosion. With increasing valve opening, both the average vorticity magnitude on the walls and the average velocity near the walls increase, which in turn leads to increased erosion on the valve stem and valve plate Sections A and B.
3. Velocity and vorticity jointly govern erosion rates on the critical components. When the valve opening degree exceeds 40%, two tapered vortex structures are observed downstream, and the vortices appear to be roughly symmetrical.

This study can be further extended to explore the correlation between erosion and flow characteristics, enhancing the understanding of erosion mechanisms. This method can be extended to identify the connection between vortices and wear patterns, informing erosion suppression strategies.

FUNDING

This work is supported by the National Natural Science Foundation of China Joint Fund of the Key Program (Grant No. U24A20111), the National Key Research and Development Program of China (Grant No. 2023YFC3008704), and the Key Research and Development Program of Shaanxi Province (Grant No. 2024GX-YBXM-268).

CONFLICTS OF INTEREST

The authors declare that they have no known competing financial interests or personal relationships that could have appeared to influence the work reported in this paper.

AUTHOR CONTRIBUTIONS

X. L. Yang: Writing review & editing, Writing original draft, Visualization, Validation, Software, Methodology, Investigation, Formal analysis, Conceptualization. **Y. J. Lü:** Writing review & editing, supervision, resources, methodology, investigation, funding acquisition, and data curation. **L. Xu:** Validation, Resources, Investigation, Data curation. **Y. S. Ma:** Resources, Funding acquisition. **R. B. Chen:** Resources. **Q. A. Li:** Resources.

REFERENCES

Chen, D. S., Jiang, J. Y., Ming, L. N., Zhang, G., Lin, Z., & Li, H. (2025). Study on gas-liquid-solid multiphase flow and erosion in ball valves, *Engineering Failure Analysis*, *167*, 108945. https://doi.org/10.1016/j.engfailanal.2024.108945

Forder, A., Thew, M., & Harrison, D. (1998). A numerical investigation of solid particle erosion experienced

within oilfield control valves. *Wear*, *216*, 184-193.

Gao, G. Y., Guo, S. S., & Li, D. R. (2024). A review of cavitation erosion on pumps and valves in nuclear power plants. *Materials*, *17*(5), 1007. https://doi.org/10.3390/ma17051007

Geng, K. H., Hu, C. X., Yang, C., & Rong, R. (2021). Numerical investigation on transient aero-thermal characteristics of a labyrinth regulating valve for nuclear power plant. *Nuclear Engineering and Design*, *382*, 111369. https://doi.org/10.1016/j.nucengdes.2021.111369

Gosman, A. D., & Ioannides, E. (1983). Aspects of computer simulation of liquid-fuelled combustors. *Journal of Energy*, *7*(6), 482-490.

Guan, A. Q., Zhong, F. P., Qiu, C., Jin, Z. J., & Qian, J. Y. (2024). Erosion wear analysis on valve cage of cage-typed sleeve control valve for coal liquefaction. *Journal of Fluids Engineering-Transactions of the ASME*, *146*(10), 101206. https://doi.org/10.1115/1.4065306

Haider, A., & Levenspiel, O. (1989). Drag coefficient and terminal velocity of spherical and nonspherical particles. *Powder Technology*, *58*, 63-70.

Hong, S. M., Peng, G. J., Yu, D. H., Chang, H., & Wang, X. K. (2023). Investigation on the erosion characteristics of liquid-solid two-phase flow in tee pipes based on CFD-DEM. *Journal of Marine Science and Engineering*, *11*(12), 2231. https://doi.org/10.3390/jmse11122231

Hunt, J. C. R., Wray, A. A., & Moin, P. (1988). Eddies, streams, and convergence zones in turbulent flows. *Summer Program of the Center for Turbulent Research*. 193-207.

Javaheri, V., Porter, D., & Kuokkala, V. T. (2018). Slurry erosion of steel-review of tests, mechanisms and materials. *Wear*, *408*, 248-273. https://doi.org/10.1016/j.wear.2018.05.010

Jin, H., Xiang, H., Wang, M., Wen, R., Liu, X., & Wang, C. (2024a). Numerical study of erosion wear characteristics in a high-pressure black water angle valve by using CFD-VOF-DPM method. *Journal of Applied Fluid Mechanics*, *17*(9), 2061-2078. https://doi.org/10.47176/JAFM.17.9.2456

Jin, H. Z., He, J., Wang, C., & Liu, X. F. (2024b). Influence of particle shape on erosive wear in liquid-solid two-phase flow of blackwater angle valves. *Powder Technology*, *448*, 120320. https://doi.org/10.1016/j.powtec.2024.120320

Kang, J., Yuan, Z. H., Li, J. C., Yang, P. F., & Liang, N. (2024a). Performance degradation model and life prediction method of spool pair caused by erosion wear. *Flow Measurement and Instrumentation*, *97*, 102610. https://doi.org/10.1016/j.flowmeasinst.2024.102610

Kang, C., Li, M. H., Teng, S., Liu, H. X., & Chen. Z. R. (2024b). Erosive wear caused by large solid particles carried by a flowing liquid: a comprehensive review. *Processes*, *12*(6), 1150. https://doi.org/10.3390/pr12061150

Khan, R., Wieczorowski, M., Seikh, A. H., & Alnaser, I. A. (2024). Experimental and numerical study of erosive wear of t-pipes in multiphase flow. *Engineering Science and Technology-An International Journal*, *52*, 101683. https://doi.org/10.1016/j.jestch.2024.101683

Li, D. B., Liu, X. C., Liao, H. H., Bing, L., Hou, P. Y., Nie, R., & Jiao, Z. X. (2024). A prediction model of fluid-solid erosion wear in hydraulic spool orifice. *Wear*, *540*, 205235. https://doi.org/10.1016/j.wear.2023.205235

Li, S.X., Zhang, B. H., Yang, L. X., Zhang, J. Z., Wang, Y. X., & Kang, W. Y. (2023). Study on wear properties of the graphite-sealing surfaces in triple eccentric butterfly valve based on EDEM-fluent coupling. *Machines*, *11*(4), 463. https://doi.org/10.3390/machines11040463

Li, Y. Z., Du, J. T., Lan, Y. J., Du, H., & Huang, H. (2022). Numerical analysis of the factors influencing the erosion of the valve port of a high-speed on/off valve. *Applied Sciences-Basel*, *12*(12), 6212. https://doi.org/10.3390/app12126212

Lin, Z. H., Li, J. Y., Jin, Z. J. & Qian, J. Y. (2021). Fluid dynamic analysis of liquefied natural gas flow through a cryogenic ball valve in liquefied natural gas receiving stations. *Energy*, *226*, 120376. https://doi.org/10.1016/j.energy.2021.120376

Lin, Z., Yu, H. B., Yu, T. C., & Zhu, Z. C. (2022). Numerical study of solid-liquid two-phase flow and erosion in ball valves with different openings. *Advanced Powder Technology*, *33*(5), 103542. https://doi.org/10.1016/j.apt.2022.103542

Liu, B., Zhao, J. G., & Qian, J. H. (2017). Numerical analysis of cavitation erosion and particle erosion in butterfly valve. *Engineering Failure Analysis*, *80*, 312-324. https://doi.org/10.1016/j.engfailanal.2017.06.045

Liu, X. Q., Qi, M. H., Ji, H., Liu, F., Lin, G., & Xiao, Y. (2024a). Orifice erosion effect and variable gain control method for hydraulic servo spool valve. *Flow Measurement and Instrumentation*, *100*, 102714. https://doi.org/10.1016/j.flowmeasinst.2024.102714

Liu, Q. T., Xie, C. H., & Cheng, B. X. (2024b). Butterfly valve erosion prediction based on LSTM network. *Flow Measurement and Instrumentation*, *98*, 102652. https://doi.org/10.1016/j.flowmeasinst.2024.102652

Ma, G. F., Lin, Z., & Zhu, Z. C. (2020). Investigation of transient gas-solid flow characteristics and particle erosion in a square gate valve. *Engineering Failure Analysis*, *118*, 104827. https://doi.org/10.1016/j.engfailanal.2020.104827

Oka, Y. I., & Yoshida, T. (2005). *Practical estimation of erosion damage caused by solid particle impact, part 2: mechanical properties of materials directly associated with erosion damage*. 15th International Conference on Wear of Materials, 259, 102-109.

Ou, G., Cao, X., Wang, C., Duan, A., & Jin, H. (2022). CFD-DEM-based numerical simulation of erosion characteristic of multistage pressure relief string regulating valve. *Journal of Applied Fluid Mechanics*, *15*(4), 999-1015. https://doi.org/10.47176/JAFM.15.04.1022

Peng, D. H., Dong, S. H., Wang, Z. Q., Wang, D. Y., Chen, Y.N, & Zhang, L. B. (2021). Characterization of the solid particle erosion of the sealing surface materials of a ball valve. *Metals*, *11*(2), 263. https://doi.org/10.3390/met11020263

Perera, P., Hayward, K., Guzzomi, F., & Vafadar, A. (2024). Erosion wear characterization of an open ductile iron butterfly valve to aluminium oxide flow. *Tribology International*, *191*, 109199. https://doi.org/10.1016/j.triboint.2023.109199

Qian, J. Y., Xu, J. X., Zhong, F. P., Lin, Z. H., Hua, T. F., & Jin, Z. J. (2023). Solid-liquid flow characteristics and sticking-force analysis of valve-core fitting clearance. *Journal of Zhejiang University-Science A*, *24*(12), 1096-1105. https://doi.org/10.1631/jzus.A2300061

Shin, T. H., Liou, W. W., Shabbir, A., Yang, Z. G., & Jiang, Z. (1995). A new k-ε eddy viscosity model for high Reynolds number turbulent flows. *Computers and Fluids*, *24*(3), 227-238.

Shokri, R., Ghaemi, S., Nobes, D. S., & Sanders, R. S. (2017). Investigation of particle-laden turbulent pipe flow at high-Reynolds-number using particle image/tracking velocimetry. *International Journal of Multiphase Flow*, *89*, 136-149. https://doi.org/10.1016/j.ijmultiphaseflow.2016.06.023

Su, G. Q., Li, Y., & Zhang, J. W. (2024). Flow accelerated corrosion and thinning mechanism of the pipeline after the butterfly valve based on CFD. *Engineering Failure Analysis*, *156*, 107844. https://doi.org/10.1016/j.engfailanal.2023.107844

Sun, X., Kim, H. S., Yang, S. D., Kim, C. K., & Yoon, J. Y. (2017). Numerical investigation of the effect of surface roughness on the flow coefficient of an eccentric butterfly valve. *Journal of Mechanical Science and Technology*, *31*(6), 2839-2848. https://doi.org/10.1007/s12206-017-0527-0

Tarodiya, R., & Levy, A. (2021). Surface erosion due to particle-surface interactions-a review. *Powder Technology*, *387*, 527-559. https://doi.org/10.1016/j.powtec.2021.04.055

Veiskarami, A., & Saidi, M. (2024). Numerical analysis of gas-solid flow erosion in different geometries as alternatives to a standard pipe elbow. *Powder Technology*, *448*, 120334. https://doi.org/10.1016/j.powtec.2024.120334

Wang, J. L., Zhang, Y. F., & Tang, H. S. (2024). Erosion wear characteristics of metal seal floating ball valve in gas-solid-liquid three-phase flow. *AIP Advance*, *14*(6), 065202. https://doi.org/10.1063/5.0210843

Wen, F. P., Xu, L. Y., Chen, Y. X., Deng, Z. F., Zhang, S., Song, W. M., Li, Y. G., & Wei, L. P. (2024). Numerical simulation of water-slag elbow erosion-inhibiting by regulating the slag injection position with a novel preceding rotating sheet structure. *Particuology*, *90*, 323-339. https://doi.org/10.1016/j.partic.2024.01.001

Xiong, J. F., Bu, Y. B., Zhang, G. J., Liu, J., Xu, G. L., & Huang, X. M. (2024). Study on a leakage rate predictive model with application in multi-conditions conversion for double-offset butterfly valves. *Nuclear Engineering and Design*, *429*, 113630. https://doi.org/10.1016/j.nucengdes.2024.113630

Xu, B. L., Lin, Z., Zhu, Z. C., & Yu, T. C. (2022). Experimental and simulation study of the effect of gravity on the solid-liquid two-phase flow and erosion of ball valve. *Advanced Powder Technology*, *33*(2), 103416. https://doi.org/10.1016/j.apt.2021.103416

Xu, B. L., Zhu, Z. C., Lin, Z., & Wang, D. R. (2021). Solid-liquid two-phase flow and erosion calculation of butterfly valves at small opening based on DEM method. *Industrial Lubrication and Tribology*, *73*(3), 414-421. https://doi.org/10.1108/ILT-07-2020-0264.

Yan, L., Ma, X., Miao, X., Wang, Y., Pang, Y., & Song, X. (2024). Numerical investigation and rapid prediction of the erosion rate of gate valve in gas-solid flow. *Powder Technology*, *448*, 120285. https://doi.org/10.1016/j.powtec.2024.120285

Yang, X. L., Lü, Y. J., Xu, L., Ma, Y. S., Chen, R. B., & Zhao, X. W. (2024). Numerical investigation on cavitation erosion and evolution of choked flow in a tri-eccentric butterfly valve. *Flow Measurement and Instrumentation*, *100*, 102725. https://doi.org/10.1016/j.flowmeasinst.2024.102725

Yin, Y. B., Yuan, J. Y., & Guo, S. G. (2017). Numerical study of solid particle erosion in hydraulic spool valves. *Wear*, *392*, 174-189. https://doi.org/10.1016/j.wear.2017.09.021

Zeng, L., Zhang, G. A. & Guo, X. P. (2014). Erosion-corrosion at different locations of X65 carbon steel elbow. *Corrosion Science*, *85*, 318-330. https://doi.org/10.1016/j.corsci.2014.04.045

Zhang, J., Yin, W. L., Wang, X., Zheng, S. W., Pan, L.J., & Zhai, F.G. (2024a). Flow field torque analysis and valve plate optimization of butterfly anti-stick bleed valve. *Flow Measurement and Instrumentation*, *100*, 102685. https://doi.org/10.1016/j.flowmeasinst.2024.102685

Zhang, G., Zhang, H. Y., Xin, J. L. Chen, D. S., & Lin, Z. (2024b). Numerical study of solid-liquid two-phase flows and erosion in a Y-type slurry valve with different seat structures. *Journal of Applied Fluid Mechanics*, *17*(8), 1657-1676. https://doi.org/10.47176/jafm.17.8.2451

Zhang, Y., Reuterfors, E. P., Mclaury, B. S., Shirazi, S. A., & Rybicki, E. F. (2007). Comparison of computed and measured particle velocities and erosion in water and air flows. *Wear*, *263*, 330-338. https://doi.org/10.1016/j.wear.2006.12.048

Zhao, L., Wu, J. Y., Jin, Z. J., & Qian, J. Y. (2022). Cavitation effect on flow resistance of sleeve regulating valve. *Flow Measurement and Instrumentation*, *88*, 102259. https://doi.org/10.1016/j.flowmeasinst.2022.102259